Graphitized activated carbon based on big bluestem as an electrode for supercapacitors

Article *in* RSC Advances · March 2014

DOI: 10.1039/c3ra46037a

6 authors, including:

Hong Jin
Xi'an Jiaotong University
9 PUBLICATIONS **357** CITATIONS
SEE PROFILE

Xiaomin Wang
Chinese Academy of Sciences
19 PUBLICATIONS **668** CITATIONS
SEE PROFILE

Zhengrong Gu
South Dakota State University
97 PUBLICATIONS **2,800** CITATIONS
SEE PROFILE

James D Hoefelmeyer
University of South Dakota
85 PUBLICATIONS **3,013** CITATIONS
SEE PROFILE

RSC Advances

PAPER

View Article Online
View Journal | View Issue

Cite this: *RSC Adv.*, 2014, **4**, 14136

Graphitized activated carbon based on big bluestem as an electrode for supercapacitors†

Hong Jin,[a] Xiaomin Wang,[a] Zhengrong Gu,*[a] James D. Hoefelmeyer,[b] K. Muthukumarappan[a] and James Julson[a]

Received 22nd October 2013
Accepted 22nd January 2014

DOI: 10.1039/c3ra46037a

www.rsc.org/advances

Activated carbon based on biochar is an attractive material for energy storage in terms of its high specific capacitance and low cost. The activated carbon samples were based on big bluestem biochar, which is the waste from a thermochemical process optimized for bio-oil production. Sodium bicarbonate, sodium hydroxide and potassium hydroxide were used as reagents to obtain the activated carbon samples. The surface area and pore structure of the activated carbon, characterized by the N_2 adsorption–desorption method, were firmly in conjunction with those of the reagents. The high specific surface area (2490 m^2 g^{-1}) of the activated carbon was achieved by the activation of potassium hydroxide. Scanning electron microscopy and Raman spectroscopy were used to test the microstructure and crystallographic orientation of the carbon samples. Concerning the G band (1580 cm^{-1}) and the ratio of this with the D band (1338 cm^{-1}), which was 0.55, the Raman spectrum indicated that the potassium hydroxide activated carbon sample contained sp^2 carbon. The 2D (2680 cm^{-1}) band showed that this activated carbon has similar properties to multilayer graphene. The cyclic voltammetry, galvanostatic charge–discharge and electrochemical impedance spectroscopy were measured after the activated carbon was assembled into supercapacitors. The potassium hydroxide activated carbon sample presented a high specific capacitance of 283 F g^{-1}, and a relatively low inner resistance of 2 ohm.

1. Introduction

Supercapacitors, which are also known as ultracapacitors, are becoming attractive due to their high power density, high energy density and long life cycle.[1–6] Normally, supercapacitors are used as intermediate energy storage devices, which show a higher energy density than traditional capacitors and a higher power density than secondary batteries.[6–8] Technically, there are generally two types of supercapacitors based on their electrode charge–discharge mechanism: electrochemical double layer capacitors (EDLC) and pseudocapacitors. Capacitance in EDLC, mostly, comes from ion storage in the porous electrodes, while in pseudocapacitance it comes from the fast reversible redox reactions in the electrodes.[9]

Carbon based materials have been studied for several years because of their high specific surface area, high specific volume and good electrical conductivity. Over the last few years, researchers have been strongly attracted to activated carbon,[10,11] carbon nanotubes,[4,12] graphene[13–15] and composites of these.[16] Carbon nanotubes and graphene are much more expensive than activated carbon. Therefore, activated carbon materials would possess much higher market potential.[17] Due to environmental protection principles, in the activated carbon field, researchers have transferred from pitch coke[5] to biomass residues. Recently, camellia oleifera shell,[1] banana peel,[10] argan (Argania spinosa) seed shells,[11] pistachio shells[18] and distillers dried grains with solubles (DDGS)[19] have been studied for producing high specific capacitance supercapacitors.

Big bluestem, which is also called Andropogon gerardii or prairie tallgrass, is the principal grass species in the Midwest United States.[20] Big bluestem has been utilized to generate biofuels through thermochemical processes. However, biochar, which is around 30% of the initial biomass, is generated in the pyrolysis process. In this work, we developed three different activated carbon samples (with specific surface areas from 524–2490 m^2 g^{-1}) based on biochar from the pyrolyzation of big bluestem. The influences of the reagents on the surface area, pore structure, degree of graphitization and elemental composition were studied thoroughly. The electrochemical properties were characterized by different instruments and the relationships between the specific capacitance and pore properties were analyzed.

[a]*Agricultural and Biosystems Engineering Department, South Dakota State University, P.O. Box 2120, 1400 North Campus Drive, AgE building, SAE 221, Brookings, SD 57007, USA. E-mail: Zhengrong.gu@sdstate.edu; Tel: +1-605-688-5372*

[b]*Chemistry department, University of South Dakota, 414 E. Clark St., Vermillion, SD 57069, USA*

† Electronic supplementary information (ESI) available. See DOI: 10.1039/c3ra46037a

2. Experimental

2.1 Preparation of activated carbon

Big bluestem biochar was used as the feeding material for carbon activation. The biochar was produced from big bluestem grass using pyrolysis processes, which were optimized for bio-oil production. $NaHCO_3$ (S1), NaOH (S2) and KOH (S3) were used as catalysts for chemical activation in an N_2 inert atmosphere, and the mechanisms of the base activation have been reported by several researchers.[21–23] Biochar samples were mixed with a 5 mol L^{-1} solution of the catalysts, soaked overnight (*i.e.* 24 hours) at room temperature and dried in a conventional oven at 120 °C overnight. These mixtures were further dried at 400 °C in a muffle furnace (with a chamber of 15 × 15 × 22 cm) in a N_2 atmosphere (N_2 flow was 500 mL min^{-1}) for more than 2 hours to remove the water of crystallization. Then the activation was carried out at a specific temperature of 820 °C for 1 hour. The activated samples were cooled to room temperature in the muffle furnace in the same N_2 atmosphere. The activated carbon samples were further purified, refluxed in 0.1 mol L^{-1} HCl, and then washed with deionized water at pH 7 and dried at 105 °C overnight under vacuum. The samples were listed as S1, S2 and S3, based on the activation reagents used.

2.2 Characterization of activated carbon

Physisorption analyses with N_2 were carried out at 77 K (liquid nitrogen bath), using an ASAP 2010 Micropore analyzer. The specific surface areas were calculated using the Brunauer–Emmett–Teller (BET) equation. The total pore volumes were obtained at the relative pressure of $P/P_0 = 0.995$. The micropore volume was estimated using the *t*-plot method, while the mesopore volume and the pore size distribution were determined by NLDFT analysis for carbon with the slit pore model (Micromeritics Inc.) based on N_2 isotherm adsorption data. The structure of activated carbon was also characterized with Raman spectroscopy (using a Horiba LABRam confocal Raman microscope) at room temperature, using an excitation wavelength at 532 nm from a diode pumped solid-state laser, as well as SEM (HITACHI S-3400N) and TEM.

2.3 Electrode preparation and electrochemical measurements

The supercapacitors were assembled using our group's previous method.[19] For all of the electrochemical characterization, the surface area of the electrode was 1 cm^2. Meanwhile, the electrolytic medium was 6 mol L^{-1} KOH. The electrodes were prepared by pressing the slurry of activated carbon, carbon black (a conducting material from Fisher scientific) and PTFE (a binder) with a mass ratio of 8 : 1 : 1 on to nickel foam. Two-electrode sandwich-type cells were built using a stainless steel coin cell (2032) with a microporous PP separator celgard-3501 between the electrodes. Two-electrode supercapacitors were assembled in an argon protected glove box.

Cyclic voltammetry (with a scan rate from 5 to 20 mV s^{-1}) and galvanostatic charge–discharge cycling (with a current density load from 0.1 to 1.0 A g^{-1}) were performed using an SP-150 multichannel potentiostat-galvanostat-EIS instrument (Biologic, France). The electrical conductivity of the supercapacitors was measured through electrochemical impedance spectroscopy (*i.e.* frequency response analysis yields over frequencies ranging from 0.1 Hz to 200 000 Hz with a potential amplitude of 10 mV), with an SP-150 multichannel potentiostat-galvanostat-EIS instrument (Biologic, France). The values of the specific capacitance were calculated from the galvanostatic discharge characteristics at current densities of 0.1 to 1.0 A g^{-1}, and expressed in farad per gram (farad per square meter was dependent on the surface area of the activated carbon in the electrode) of the electrode's active material.

The specific capacitance of the electrode was calculated using eqn (1) (ref. 24)

$$C = \frac{2I\Delta t}{m\Delta V} \quad (1)$$

Where I is the charge or discharge current density, Δt is the corresponding charge or discharge time, m is the mass of one of the symmetrical electrodes, and ΔV is the total corresponding potential change.

3. Results and discussion

3.1 Physiochemical characterization of activated carbon

The pore structure and the surface area parameters were obtained by the N_2 adsorption method, while the micropore volume was determined using density functional theory (DFT). As is shown in Table 1, the pore structures and the surface areas are largely affected by the type of activation reagents used. Activation with potassium hydroxide reported the best properties for carbon among the three reagents utilized. With a dosage of 0.05 mol g^{-1} (ratio between the mass of the reagent and the biochar), sodium bicarbonate can only generate a biochar with a surface area of 552 m^2 g^{-1}, while the biochar activated with sodium hydroxide generated a surface area of 1616 m^2 g^{-1}. However, the surface area of S3, which was produced using potassium hydroxide as the catalyst, created a biochar with a surface area of 2490 m^2 g^{-1}.

Table S1 in the ESI † also reports the surface areas attained by each activation reagent at the ratio of 0.025 mol g^{-1}. S1-1, which was obtained by sodium bicarbonate activation, reports a surface area of 524 m^2 g^{-1}. This surface area is nearly identical to that of the sample created by 0.05 mol g^{-1} sodium bicarbonate. S2-1 presents an extremely low surface area of 376 m^2 g^{-1}, while S3-1 also presents a relatively low surface area. As is indicated by the observations of the three activation reagents, the surface area of the samples are affected by the reagent/biochar ratio during activation. The observed correlation dictates that within the range of this reagent/biochar ratio, the surface area will increase as the reagent/biochar ratio increases.

The isothermal curves are shown in Fig. 1. All of the samples displayed a typical H2 hysteresis loop between the relative pressures of 0.4–1.0. S3 presented a higher quantity adsorption than S1 and S2, which means that S3 adsorbs more nitrogen gas than S1 and S2; in other words, S3 has the highest pore volume, as is shown in Table 1. The detailed pore distributions are

Table 1 Surface area and pore-structure parameters of the activated carbon

Sample #	Catalysts	S_{BET}[a] $m^2\ g^{-1}$	V_T[b] $cm^3\ g^{-1}$	V_{micro}[c] $cm^3\ g^{-1}$	$d_{average}$[d] nm
S1	$NaHCO_3$	552	0.38	0.13	3.0
S2	NaOH	1616	0.86	0.38	2.1
S3	KOH	2490	1.7	0.43	2.5

[a] BET (Brunauer–Emmett–Teller) surface area. [b] Total pore volume, measured at $P/P_0 = 0.995$. [c] Micropore volume, based on density functional theory (DFT). [d] Average pore diameter of activated carbon samples, calculated by 4 V_T/S_{BET}.

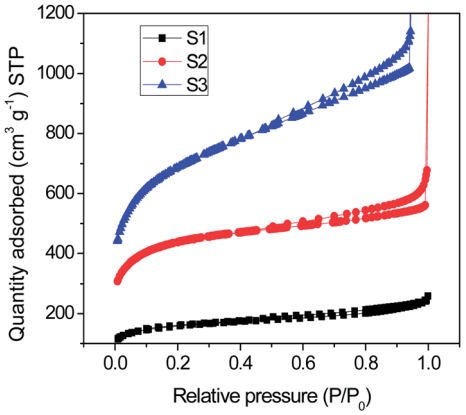

Fig. 1 Adsorption and desorption isotherm of nitrogen at 77 K, on the activated carbon.

presented in Fig. 2. Three of the above samples showed a peak at a pore width of 4.0 nm, and a peak at the pore width of 32 nm was also present in S3. The possible reason for this is that potassium hydroxide is much stronger than both sodium hydroxide and sodium bicarbonate for activating the biochar. Therefore, the original 4.0 nm pore structure was progressively broken down to form a higher width pore structure; as a result, the pore distribution of S3 not only presents the peak of 4.0 nm, but also a pore width of 32 nm.

The SEM images and Raman spectra are presented in Fig. 3. The SEM images of the three samples show the different microstructures. The variance between S1 and S2 is not that apparent; however, it is also clear that the sodium hydroxide activation reagent generated more small particles than the sodium bicarbonate. The SEM image (Fig. 3C) of the microstructure of S3 indicates that part of the big bluestem biochar is cracked into small particles and the other part of the biochar is cleaved into a platelike structure. The Raman spectra are shown in Fig. 3D. All three of the samples present partial graphite characteristics, as shown in the spectra. The spectra of S1 and S2 demonstrate that both of these samples could have incomplete graphite properties due to the G band peak. However, the higher intensity ratio of the D band *versus* the G band (I_D/I_G) of S1 (2.64) and S2 (4.54) means that these two samples contain more disordered carbon materials. The intensity ratio of S3 is just 0.55, and the spectrum of S3 shows a 2D overtone mode, which means that S3 is not just a highly ordered graphite material, but also contains a multilayer graphene structure.[25]

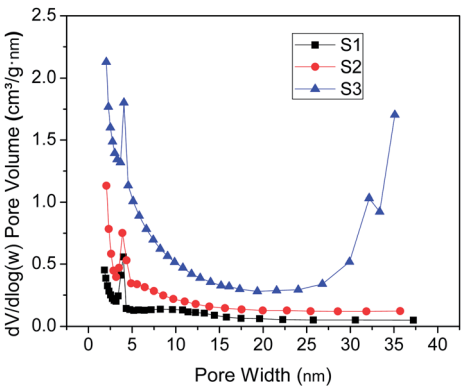

Fig. 2 Pore size distributions of the activated carbon.

The TEM images are displayed in Fig. 4. The more detailed microstructures of these three samples can be obtained from the TEM images. As shown in Fig. 4A and B, S1 and S2 are fully occupied by nanoporous activated carbon structures, which coincide with the BET results. However, S3 not only contains nanoporous structures as shown in Fig. 4D, but also has several layers of graphene structures as shown in Fig. 3C, which coincide with the Raman spectroscopy result.

3.2 Electrochemical performances of activated carbon

Galvanostatic charge–discharge was used to test the performance of the supercapacitors based on the activated carbons. The supercapacitors S1 and S3 present excellent capacitor characteristics; in the lower current of 0.1 A g^{-1}; however, as shown in Fig. 5A, S2 does not show an excellent isosceles triangle curve. The voltage drops sharply when the supercapacitor S2 starts to discharge, and the initiating charging voltage is 0.1 V. This is probably because of the lower average pore diameter, as shown in Table 1. Due to the charge–discharge process, the ions would transport from the electrolyte solution into the electrode's inner pore surface. The pore structure, especially the pore diameter, would be the key factor affecting the transportation. The smaller pore diameter would prevent the ions from intercalating to the inner pore surface; in other words, the resistance of the supercapacitor would become higher than the other two samples due to the lower pore diameter. Finally, with a charge–discharge current density of 0.1 A g^{-1}, the electrolyte ions would need more time to migrate; that is to say, the voltage drop (*IR*: *I*, current; *R*, resistance) would occur. Therefore, in Fig. 5A, S2 presents a sharp drop when the supercapacitor starts to discharge.

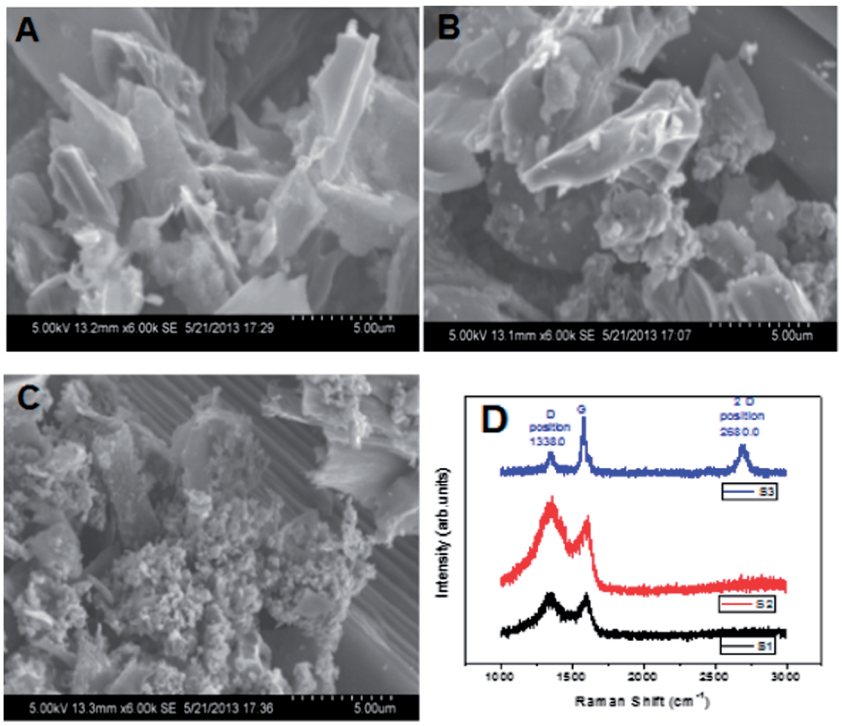

Fig. 3 SEM images and Raman spectra of the activated carbon. (A) SEM image of S1 (B) SEM image of S2 (C) SEM image of S3 (D) Raman spectra of the activated carbon.

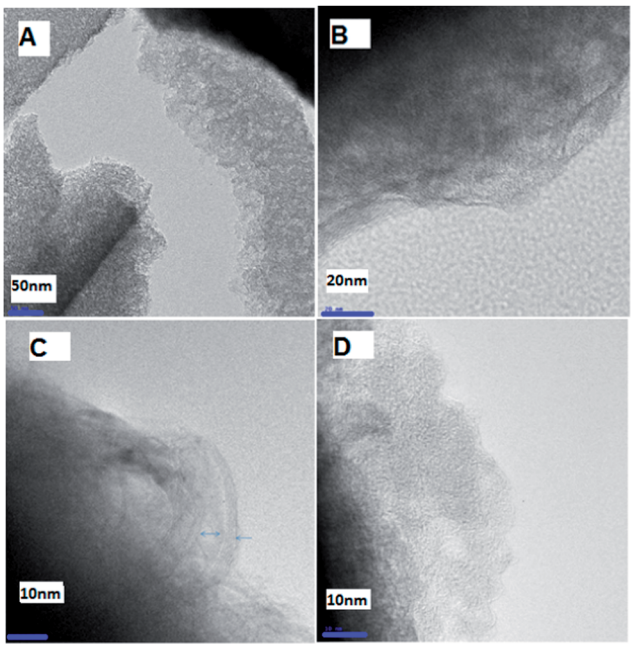

Fig. 4 TEM images of the activated carbon. (A) TEM image of S1 (B) TEM image of S2 (C & D) TEM image of S3.

The curves of charge–discharge of the supercapacitors at 0.5 A g^{-1} are shown in Fig. 5B. The specific capacitance of S2 is even less than S1, which can be explained as follows: at this higher current density, ion transport in the capacitor system becomes more important and the higher percentage of 4.0 nm pores supply a sufficient transportation pathway for the ions arriving at the micropore's surface. At a current density of 1.0 A g^{-1}, the specific capacitance of S1 becomes much higher than that of the sample S2, and the specific capacitance of S3 is still much higher than both S1 and S2. As is shown in Fig. 2, the pore structure of S3 is hierarchically distributed, and not only contains the 4.0 nm pores, but also plenty of 32 nm pores. Therefore, the charge–discharge curves of S3 are all excellent isosceles triangle curves, and because of the higher specific surface area, the specific capacitances of S3 at different current densities are higher than for the other two samples. Fig. 5D presents the relationship between the specific capacitance and current density, and the charge and discharge cycle details are shown in the ESI (Fig. S1–S3).† The specific capacitance decreases while the current density increases for all three samples. The specific capacitance of S2 decreases distinctively (from 173 to 68 F g^{-1}) as the current density increases from 0.1 to 1.0 A g^{-1}. On the other hand, the specific capacitances of S1 and S3 do not decrease that much, especially S1, which still presents 87% specific capacitance upon increasing the density from 0.1 to 1.0 A g^{-1}. Even though the specific capacitance of S3 decreases from 283 F g^{-1} to 184 F g^{-1} as the current density increases from 0.1 to 1.0 A g^{-1}; it is still higher than the specific capacitances of S1 and S2 at the smaller current density of 0.1 A g^{-1}. All of the results have a close relationship with the activated carbon properties. At the lowest current density of 0.1 A g^{-1}, the specific capacitance is affected more by surface area than pore size. Therefore, the sequence of the specific capacitances follows the sequence of surface areas. As the current density increases, the system

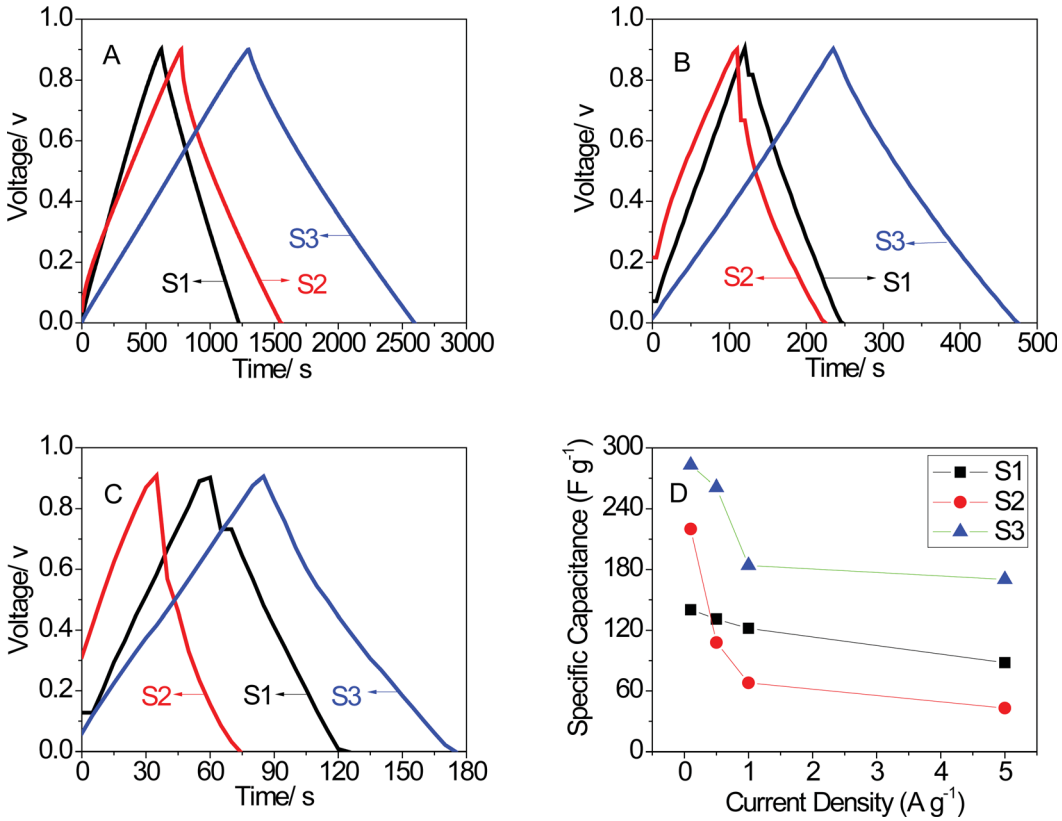

Fig. 5 Galvanostatic charge–discharge specific capacitance. (A) Current density of 0.1 A g^{-1}, (B) current density of 0.5 A g^{-1}, (C) current density of 1.0 A g^{-1}, (D) the relationship between the area specific capacitance and current density.

requires larger sized pores to support a faster ion transport. As a result of its smaller pore size (2.1 nm), the specific capacitance of S2 becomes less than that of S1 even though the surface area of S2 is much higher than that of S1. This could be confirmed by increasing the current density to 1.0 A g^{-1} and comparing S2 and S1. As shown in Fig. 5D, sample S3 retains 92.2% of its specific capacitance on increasing the current density from 0.1 A g^{-1} to 0.5 A g^{-1}. However, it maintains 70.5% as the current density increases from 0.5 A g^{-1} to 1.0 A g^{-1}. On the other side, the specific capacitances of S1 are more stable over a wider range of current densities, being 93.6% (0.1 A g^{-1} to 0.5 A g^{-1}) and 93.1% (0.5 A g^{-1} to 1.0 A g^{-1}). This is because the average pore sizes of S3 (2.5 nm) and S1 (3.0 nm) are higher than that of S2. For the first part, the specific capacitance decrease of both S3 and S1 is not that obvious; however, for the second part, with the current density continuously increasing, S3 does not have a large enough pore structure to support fast ion transport, so eventually, the specific capacitance of S3 greatly decreases. When the current density continuously increases to the high density of 5.0 A g^{-1}, the specific capacitance of S3 does not decrease much. This is due to its good conductivity and the presence of large pores (~32 nm). We compared our results with several other researchers who are looking for high quality carbon materials for supercapacitors. As Table 2 shows, the functionalized activated carbon from coconut shell[26] at a very low scan rate of 10 mV s^{-1} shows a specific capacitance of 154 F g^{-1}. The CVD generated mesoporous carbon from ethylene[27] shows a specific capacitance of 99 F g^{-1} at the low current density of 0.2 A g^{-1}. Even chemically modified graphene[15] presents just 135 F g^{-1} at a current density of 1.3 A g^{-1}. Thus, the graphitized carbon from big bluestem is competitive as an electrode material for application in supercapacitors.

Cyclic voltammetry (CV) was performed to characterize the properties of the supercapacitors based on the various samples of activated carbon. The CV curves are all basically rectangular shaped, without noticeable reaction peaks, similar to an ideal supercapacitor,[28] especially at the lower scanning rate of 5 mV s^{-1}. As is shown in Fig. 6, S3 presents a higher specific capacitance over the wide range of scanning rates, and S1 presents the best rectangular shape. The reason for this is the same as explained in the previous paragraph. Electrochemical impedance spectra (EIS) were obtained to deeply study the electrochemical properties of the carbon material, and these were used to test the resistance of the supercapacitors. The complex-plane impedances of the activated carbon in 6 M KOH electrolytes are shown in Fig. 6D, which shows the impedances over a frequency range of 0.1–200 000 Hz. In the high frequency region, the electrochemical system could be considered a resistor, and the total resistance covers the resistance of mass transfer and electrochemical reactions, the electrolyte resistance and the resistance of the carbon matrix. The semicircle, in the high frequency region, indicates the electrode, electrolyte properties and the contact resistance. As shown in Fig. 6D, all three curves

Table 2 Specific capacitance parameters of different carbon materials

Carbon resource	Carbon type/methods	Capacitance F g^{-1} (electrolytes)	Current density A g^{-1}	Literature
Coconut shell	Functionalized AC nanoparticles	154 (1 M Na_2SO_4)	10 mV s^{-1}	Y. Jang
Ethylene	Mesoporous carbon	99 (1 M H_2SO_4)	0.2	X. Chen
Graphene	Chemically modified graphene	135 (5.5 M KOH)	1.3	M. D. Stoller
Big bluestem	Graphitized activated carbon	283 (6 M KOH)	0.1	This work
		172 (6 M KOH)	5.0	

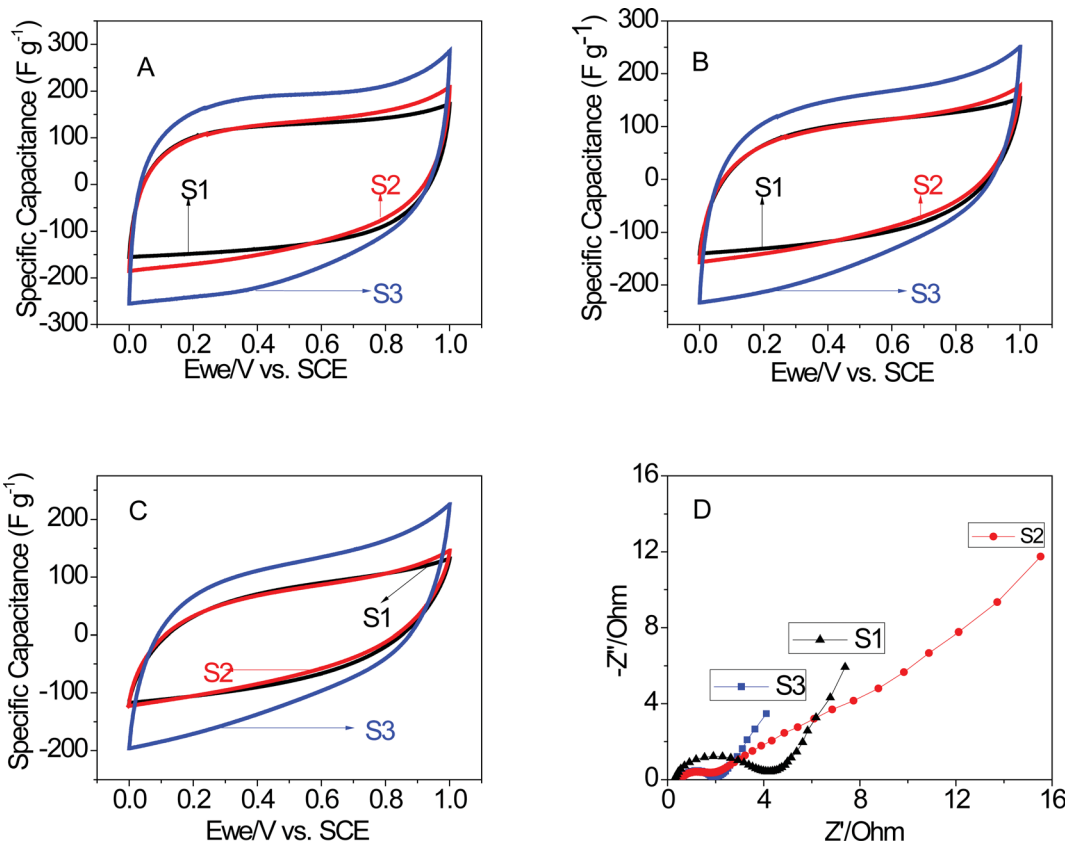

Fig. 6 Cyclic voltammograms and electrochemical impedance spectra (EIS) of activated carbon electrodes. (A) The potential scan rate of 5 mV s^{-1}, (B) the potential scan rate of 10 mV s^{-1}, (C) the potential scan rate of 20 mV s^{-1}, (D) Nyquist plots for the activated carbon in 6 M KOH electrolytes recorded at room temperature.

have nearly the same first point of intersection with the horizontal axis, because all of the supercapacitors were using 6 M KOH as the electrolyte and the same assembly method was used for all three; and normally the first intersection point reflects the resistance caused by the electrolyte and the contact resistance. Nevertheless, the second intersection points of the semicircles and the horizontal axis are different. Fig. 6D indicates that S3 presents a slightly lower intersection point than S2, and S1 presents a much higher intersection point than S2 and S3. This is because of the properties of the activated carbon, as the Raman spectra show. S1 presents two smaller peaks of the D and G bands, and does not have the same 2D band as S3, and therefore the conductivity of S1 would be worse than that of S2 and S3. The slope of the linear part in the low frequency region reflects the capacitor properties; technically, a sharper slope means a better capacitor. As shown in Fig. 6D, S3 and S1 present a similar linear line, which is much sharper than that of S2. As a result, S3 and S1 present better galvanostatic charge–discharge and cyclic voltammetry electrochemical properties than S2, which is in accordance with the results explained in this and the previous paragraph.

4. Conclusion

Big bluestem was selected as an activated carbon resource. The samples' properties depended on the type and amount of activation reagents used. KOH (where the KOH/biochar ratio equals 0.05 mol g^{-1}) was not only the best reagent for obtaining the highest specific surface area of 2490 m^2 g^{-1}, but it could also generate carbon structures similar to multilayer graphene. In a

6 M KOH aqueous solution, a high specific capacitance of 283 F g^{-1} was obtained. The specific capacitance was mainly affected by the surface area of the activated carbon, and the pore size greatly affected the specific capacitance at a high current density. The electrochemical properties reflected that the pathway for developing better carbon for supercapacitors would be through developing activated carbon with proper pore structure which is more highly conductive.

Acknowledgements

This research is funded by the project "DEVELOPMENT OF HIGH VALUE CARBON BASED ADSORBENTS FROM THERMOCHEMICALLY PRODUCED BIOCHAR" 2011-67009-20030 USDA-NIFA Agriculture and Food Research Initiative Sustainable Bioenergy Program. Purchase of the TEM was made possible by funding from the National Science Foundation (CHE-0840507).

References

1 J. Zhang, L. Gong, K. Sun, J. Jiang and X. Zhang, *J. Solid State Electrochem.*, 2012, **16**, 2179–2186.
2 W. Zhang, Z.-H. Huang, G. Cao, F. Kang and Y. Yang, *J. Power Sources*, 2012, **204**, 230–235.
3 V. Ruiz, C. Blanco, R. Santamaría, J. M. Ramos-Fernández, M. Martínez-Escandell, A. Sepúlveda-Escribano and F. Rodríguez-Reinoso, *Carbon*, 2009, **47**, 195–200.
4 C. Li, D. Wang, T. Liang, X. Wang and L. Ji, *Mater. Lett.*, 2004, **58**, 3774–3777.
5 S. Mitani, S.-I. Lee, S.-H. Yoon, Y. Korai and I. Mochida, *J. Power Sources*, 2004, **133**, 298–301.
6 Y. Z. Wei, B. Fang, S. Iwasa and M. Kumagai, *J. Power Sources*, 2005, **141**, 386–391.
7 X. Zhao, H. Tian, M. Zhu, K. Tian, J. J. Wang, F. Kang and R. A. Outlaw, *J. Power Sources*, 2009, **194**, 1208–1212.
8 E. Pollak, N. Levy, L. Eliad, G. Salitra, A. Soffer and D. Aurbach, *Isr. J. Chem.*, 2008, **48**, 287–303.
9 G. Wang, L. Zhang and J. Zhang, *Chem. Soc. Rev.*, 2012, **41**, 797–828.
10 Y. Lv, L. Gan, M. Liu, W. Xiong, Z. Xu, D. Zhu and D. S. Wright, *J. Power Sources*, 2012, **209**, 152–157.
11 A. Elmouwahidi, Z. Zapata-Benabithe, F. Carrasco-Marin and C. Moreno-Castilla, *Bioresour. Technol.*, 2012, **111**, 185–190.
12 M. F. De Volder, S. H. Tawfick, R. H. Baughman and A. J. Hart, *Science*, 2013, **339**, 535–539.
13 Y. Zhu, S. Murali, M. D. Stoller, K. J. Ganesh, W. Cai, P. J. Ferreira, A. Pirkle, R. M. Wallace, K. A. Cychosz, M. Thommes, D. Su, E. A. Stach and R. S. Ruoff, *Science*, 2011, **332**, 1537–1541.
14 Y. Huang, J. Liang and Y. Chen, *Small*, 2012, **8**, 1805–1834.
15 M. D. Stoller, S. Park, Y. Zhu, J. An and R. S. Ruoff, *Nano Lett.*, 2008, **8**, 3498–3502.
16 H. Guo and Q. Gao, *J. Power Sources*, 2009, **186**, 551–556.
17 E. Frackowiak, *Phys. Chem. Chem. Phys.*, 2007, **9**, 1774–1785.
18 C.-C. Hu, C.-C. Wang, F.-C. Wu and R.-L. Tseng, *Electrochim. Acta*, 2007, **52**, 2498–2505.
19 H. Jin, X. Wang, Z. Gu and J. Polin, *J. Power Sources*, 2013, **236**, 285–292.
20 J. Gan, W. Yuan, L. Johnson, D. Wang, R. Nelson and K. Zhang, *Bioresour. Technol.*, 2012, **116**, 413–420.
21 X. W. Zhengrong Gu, *American Transactions on Engineering & Applied Sciences*, 2012, **2**, 15–34.
22 K. Y. Foo and B. H. Hameed, *Bioresour. Technol.*, 2011, **102**, 9814–9817.
23 R. L. Tseng, *J. Hazard. Mater.*, 2007, **147**, 1020–1027.
24 Y. Gao, V. Presser, L. Zhang, J. J. Niu, J. K. McDonough, C. R. Pérez, H. Lin, H. Fong and Y. Gogotsi, *J. Power Sources*, 2012, **201**, 368–375.
25 A. K. Ray, R. K. Sahu, V. Rajinikanth, H. Bapari, M. Ghosh and P. Paul, *Carbon*, 2012, **50**, 4123–4129.
26 Y. Jang, J. Jo, Y.-M. Choi, I. Kim, S.-H. Lee, D. Kim and S. M. Yoon, *Electrochim. Acta*, 2013, **102**, 240–245.
27 X. Chen, K. Kierzek, K. Cendrowski, I. Pelech, X. Zhao, J. Feng, R. J. Kalenczuk, T. Tang and E. Mijowska, *Colloids Surf., A*, 2012, **396**, 246–250.
28 Z. Jin, W. Mu, C. Zhang, T. He, Q. Zhang, J. Hou and K. Cai, *Electrochim. Acta*, 2012, **59**, 100–104.

